Science Advances
AAAS

Supplementary Materials for

Focusing of in-plane hyperbolic polaritons in van der Waals crystals with tailored infrared nanoantennas

Javier Martín-Sánchez*, Jiahua Duan, Javier Taboada-Gutiérrez, Gonzalo Álvarez-Pérez, Kirill V. Voronin, Iván Prieto, Weiliang Ma, Qiaoliang Bao, Valentyn S. Volkov, Rainer Hillenbrand, Alexey Y. Nikitin, Pablo Alonso-González*

*Corresponding author. Email: javiermartin@uniovi.es (J.M.-S.); pabloalonso@uniovi.es (P.A.-G.)

Published 8 October 2021, *Sci. Adv.* **7**, eabj0127 (2021)
DOI: 10.1126/sciadv.abj0127

This PDF file includes:

S1. Analytical calculation of the near-field distribution of propagating phonon polaritons (PhPs) in α-MoO_3, and the focal distance of metallic nanoantennas used in this work.

In this section, we present the analytical calculation of the near-field distribution of PhPs propagating in α-MoO_3 biaxial slabs when disk or rod-like trapezoidal gold nanoantennas are used as excitation sources. The analytical expressions to extract the focal distance for each kind of nanoantenna are provided. Note that in this section x-axis and y-axis refer to directions [100] and [001] in α-MoO_3, respectively.

In these calculations, we make several assumptions: firstly, a thin-film approximation is used, under which the biaxial slab is treated as a 2D-conductivity layer (see below). Second, we assume that the exciting electric field is parallel to the out-of-plane axis (z-axis) and localized at the edges of the nanoantennas. This is reasonable since the skin depth for Au at this frequency is about 24 nm. Therefore, we will consider only the z-component of the electric field in all our derivations. Finally, we assume that the focal distance is much larger than the wavelength of the polaritons.

2D conductivity layer approximation

We model the α-MoO_3 slab as a 2D conductivity layer with zero thickness. This approximation avoids the calculation of the fields inside the slab and has been proven valid for α-MoO_3 layers with a thickness that is much smaller than the polariton wavelength *(21,36)*. The effective conductivity tensor $\hat{\sigma}_{eff}$ for the α-MoO_3 layer is related to the (2 × 2) permittivity tensor $\hat{\varepsilon} = \mathrm{diag}(\varepsilon_{xx}, \varepsilon_{yy})$ as follows: $\hat{\sigma}_{eff} = (cd/2i\lambda_0)\hat{\varepsilon}$, where c is the speed of light, d is the thickness of the layer and λ_0 is the free-space wavelength. We will also introduce the normalized conductivity tensor $\hat{\alpha} = 2\pi\hat{\sigma}_{eff}/c$ for convenience.

Dyadic Green's function for the 2D-conductive layer

To calculate the distribution of the electric field created by an extended source, such as disks or rod-like nanoantennas (not a dipole point-like source), in general, we need to solve a non-homogenous linear differential equation (non-homogeneous wave equation) of the symbolic form $\hat{\mathcal{L}}f = f_0$, where $\hat{\mathcal{L}}$ is a linear differential operator, f_0 is the "initial condition" (source), and f is the variable (representing the electric field) to be calculated. To solve this non-homogeneous equation, we can make use of the Green's function formalism (analogously to the Huygens principle in the case of propagating waves). To that end, we calculate the Green's function, $G(\boldsymbol{r} - \boldsymbol{r'})$, for the linear differential operator and get an electric field distribution as the convolution of this function with the initial field: $f(\boldsymbol{r}) = \iiint d^3\boldsymbol{r'} G(\boldsymbol{r} - \boldsymbol{r'}) f_0(\boldsymbol{r'})$. Note that the physical meaning of the Green´s function is the field created at the point with radius-vector $\boldsymbol{r}$ by the point source placed at the point $\boldsymbol{r'}$. The Green´s function is also related to the local density of photonic states (LDOS). Applying a Fourier transformation to the equation for $f(\boldsymbol{r})$, we obtain $f(\boldsymbol{k}) = G(\boldsymbol{k}) f_0(\boldsymbol{k})$, that means that $G(\boldsymbol{k})$ describes an efficiency of excitation of the mode with momentum $\boldsymbol{k}$, and is also related to the density of optical states (DOS). As we deal with the vector field, we consider the generalization of the Green's function, the dyadic Green's function (DGF), $\hat{G}(\boldsymbol{r} - \boldsymbol{r'})$, constructed for the vectorial wave equation. Using the DGF, the overall electric field of polaritons emitted by an antenna edge and propagating along the film can be calculated at any point near the film according to the Lippmann-Schwinger integral equation:

$$\boldsymbol{E}(\boldsymbol{r}) = k_0^2 \int d^3\boldsymbol{r}' \hat{G}(\boldsymbol{r} - \boldsymbol{r}')\, \boldsymbol{E_0}(\boldsymbol{r}'), \tag{1}$$

where $\boldsymbol{E}(\boldsymbol{r})$ is the field created by the source at the point $\boldsymbol{r}$, $\boldsymbol{E_0}(\boldsymbol{r}')$ is the initial field (at the surface of the source), $k_0 = \omega/c$ is the wavevector in a vacuum, ω is an angular frequency of the waves, and c is the speed of light. As we consider only z-components of the electric fields everywhere, we need only the zz-component of the DGF.

Since the s-polarized plane wave in the dielectric medium has zero projection on the z-axis, we consider only the contribution of the p-polarized waves to the DGF, which we denote as $\hat{G}_{pp}$. The latter simply provides the p-polarized component of the electromagnetic wave excited by a p-polarized point source. The DGF corresponding to the field "transmitted" through the layer is given by the following equation:

$$\hat{G}_{pp}(\boldsymbol{r} - \boldsymbol{r}') = \frac{i}{8\pi^2} \int \frac{d^2\boldsymbol{k}_{||}}{k_{1z}} e^{i\boldsymbol{k}_{||}\Delta\boldsymbol{r}_{||}} T^{pp} \langle r|k_{2p}^-\rangle\langle k_{1p}^-|r'\rangle\, e^{i(k_{1z}z' - k_{2z}z)} \tag{2}$$

where $k_{iz} = \sqrt{k_0^2\varepsilon_i - k_{||}^2}$ are the z-components of the wavevector, $\boldsymbol{k}_{||}$ is the in-plane component of the wavevector, $\Delta\boldsymbol{r}_{||}$ is the in-plane component of $\boldsymbol{r} - \boldsymbol{r}'$, ε_i $(i = 1,2)$ is the dielectric permittivity of the surrounding media (being "1" the superstrate and "2" the substrate), T^{pp} is the Fresnel's transmission coefficient, and $|k_{ip}^-\rangle$ is the basis vectors in Dirac notations for the electric field. In coordinate representation, we can write the basis vectors as follows:

$$\langle r|k_{ip}^-\rangle = \frac{k_{iz}}{k_{||}k_0\sqrt{\varepsilon_i}} \begin{pmatrix} k_x \\ k_y \\ \dfrac{k_{||}^2}{k_{iz}} \end{pmatrix} \quad \text{and} \quad \langle k_{1p}^-|r'\rangle = \frac{k_{iz}}{k_{||}k_0\sqrt{\varepsilon_i}} \begin{pmatrix} k_x & k_y & \dfrac{k_{||}^2}{k_{iz}} \end{pmatrix} \tag{3}$$

Consequently, $\langle r|k_{2p}^-\rangle\langle k_{1p}^-|r'\rangle$ is given by the following dyadic:

$$\langle r|k_{2p}^-\rangle\langle k_{1p}^-|r'\rangle = \frac{k_{1z}k_{2z}}{k_{||}^2k_0^2\sqrt{\varepsilon_1\varepsilon_2}} \begin{pmatrix} k_x^2 & k_xk_y & \dfrac{k_xk_{||}^2}{k_{1z}} \\ k_xk_y & k_y^2 & \dfrac{k_yk_{||}^2}{k_{1z}} \\ \dfrac{k_xk_{||}^2}{k_{2z}} & \dfrac{k_yk_{||}^2}{k_{2z}} & \dfrac{k_{||}^4}{k_{1z}k_{2z}} \end{pmatrix} \tag{4}$$

Thus, for zz-component we obtain:

$$G_{zz}(\boldsymbol{r}, \boldsymbol{r}') = \frac{i}{8\pi^2k_0^2\sqrt{\varepsilon_1\varepsilon_2}} \int d^2\boldsymbol{k}_{||} G_{zz}(k_x, k_y) e^{i(k_{1z}z' - k_{2z}z)} e^{i\boldsymbol{k}_{||}\Delta\boldsymbol{r}_{||}} \tag{5}$$

where

$$G_{zz}(k_x, k_y) = \frac{k_{||}^2}{k_{1z}} T^{pp} \quad (6)$$

The Fresnel's coefficients T^{pp} can be straightforwardly obtained from Maxwell's equations. We can apply the following boundary conditions to match the in-plane components of the magnetic and electric fields at the interface between the upper medium (denoted by "1") and the lower medium (denoted by "2"):

$$\boldsymbol{E}_{1t}(x, y, 0) = \boldsymbol{E}_{2t}(x, y, 0) \quad (7)$$

$$[\boldsymbol{e}_z \times (\boldsymbol{H}_{1t}(x, y, 0) - \boldsymbol{H}_{2t}(x, y, 0))]_t = \frac{4\pi}{c} \hat{\sigma} \boldsymbol{E}_t(x, y, 0) \quad (8)$$

where $\boldsymbol{e}_z$ is the unit vector along the z-axis, $\hat{\sigma}$ is the 2D-conductivity tensor, that could be defined as $\hat{\sigma} = \frac{k_0 d \hat{\varepsilon}}{2i}$, where $\hat{\varepsilon}$ is the dielectric permittivity tensor restricted on the xy-plane, and d is the thickness of the slab *(36)*.

The fields above and below the 2D layer are given by:

$$\boldsymbol{E}_1(x, y, 0) = \frac{k_{1z}}{k_0 \sqrt{\varepsilon_1}} \begin{pmatrix} k_x \\ k_y \\ \frac{k_{||}^2}{k_{1z}} \end{pmatrix} e^{i(k_x x + k_y y)} + R^{sp} \begin{pmatrix} -k_y \\ k_x \\ 0 \end{pmatrix} e^{i(k_x x + k_y y)} + R^{pp} \frac{k_{1z}}{k_0 \sqrt{\varepsilon_1}} \begin{pmatrix} k_x \\ k_y \\ -\frac{k_{||}^2}{k_{1z}} \end{pmatrix} e^{i(k_x x + k_y y)} \quad (9)$$

$$\boldsymbol{E}_2(x, y, 0) = T^{sp} \begin{pmatrix} -k_y \\ k_x \\ 0 \end{pmatrix} e^{i(k_x x + k_y y)} + T^{pp} \frac{k_{2z}}{k_0 \sqrt{\varepsilon_2}} \begin{pmatrix} k_x \\ k_y \\ \frac{k_{||}^2}{k_{2z}} \end{pmatrix} e^{i(k_x x + k_y y)} \quad (10)$$

where R^{sp} and T^{sp} are the ratios of the amplitudes of the "reflected" and "transmitted" s-polarized waves respectively to the amplitude of the initial p-polarized wave; R^{pp} and T^{pp} are the ratios of the amplitudes of the reflected and transmitted p-polarized waves respectively to the amplitude of the initial p-polarized wave. Multiplying equation (7) by $\langle s| \equiv (-q_y \quad q_x) e^{-ik_x x - ik_y y}$, where $\boldsymbol{q} = \boldsymbol{k}/k_0$, we obtain $R^{sp} = T^{sp}$. Multiplying equation (7) by $\langle p| \equiv (q_x \quad q_y) e^{-ik_x x - ik_y y}$, we obtain $1 + R^{pp} = T^{pp} \frac{k_{2z}}{k_{1z}} \sqrt{\frac{\varepsilon_1}{\varepsilon_2}}$.

Substituting $\boldsymbol{H} = \frac{1}{k_0} \boldsymbol{k} \times \boldsymbol{E}$ into the equation (8) we obtain:

$$\boldsymbol{E}_{1z} \boldsymbol{k}_{1t} - \boldsymbol{E}_{1t} k_{1z} - \boldsymbol{E}_{2z} \boldsymbol{k}_{2t} + \boldsymbol{E}_{2t} \boldsymbol{k}_{2z} = 2 \hat{\alpha} k_0 \boldsymbol{E}_{2t} \quad (11)$$

where $\hat{\alpha} = \frac{2\pi}{c} \hat{\sigma}$ is the normalized conductivity tensor. Multiplying equation (11) by $\langle s|$ we obtain:

$$T^{sp} = T^{pp} \frac{2 k_x k_y k_{2z} (\alpha_x - \alpha_y)}{\sqrt{\varepsilon_2} k_{||}^2 (k_{1z} + k_{2z} + \frac{2k_0}{k_{||}^2} [\alpha_x k_y^2 + \alpha_y k_x^2])} \quad (12)$$

Finally, by multiplying equation (11) by $\langle p|$ and after some algebraic transformations, we obtain the Fresnel's coefficient $T^{pp}$and $G_{zz}(k_x, k_y)$ becomes:

$$G_{zz}(k_x,k_y) = \frac{k_0 k_{||}^4}{k_{1z}k_{2z}} \frac{\sqrt{\varepsilon_1\varepsilon_2}\left(\alpha_x k_y^2+\alpha_y k_x^2+k_{||}^2\frac{k_{1z}+k_{2z}}{2k_0}\right)}{\left(\alpha_x k_y^2+\alpha_y k_x^2+k_{||}^2\frac{k_{1z}+k_{2z}}{2k_0}\right)\left(\alpha_x k_x^2+\alpha_y k_y^2+\frac{k_0 k_{||}^2}{2}\left[\frac{\varepsilon_1}{k_{1z}}+\frac{\varepsilon_2}{k_{2z}}\right]\right)-k_x^2k_y^2(\alpha_x-\alpha_y)^2} \quad (13)$$

Note that the poles of $G_{zz}(k_x, k_y)$ in Eq. (13) provide the dispersion relation for polaritons in the 2D-conductivity layer *(21,36)*.

Assuming that the point source and the "probing" point (at which we wish to know the value of the electromagnetic fields) are located in the same semi-infinite half-space, the "reflected" DGF must be used instead transmitted DGF. However, the electromagnetic fields of propagating polaritons (the eigenmodes supported by our 2D layer) are mainly determined by the poles of the Fresnel coefficients (and thus the poles of the DGF). Consequently, we can safely neglect the unity in the expression $1+R^{pp} = T^{pp}\frac{k_{2z}}{k_{1z}}\sqrt{\frac{\varepsilon_1}{\varepsilon_2}}$, and therefore approximate $R^{pp} \approx T^{pp}\frac{k_{2z}}{k_{1z}}\sqrt{\frac{\varepsilon_1}{\varepsilon_2}}$ so that

$$G_{Rzz}(\boldsymbol{r},\boldsymbol{r'}) \approx \frac{-i}{8\pi^2 k_0^2\sqrt{\varepsilon_1\varepsilon_2}}\int d^2\boldsymbol{k}_{||}\frac{k_{||}^2}{k_{1z}}T^{pp}\frac{k_{2z}}{k_{1z}}e^{i(k_{1z}z'+k_{2z}z)}e^{i\boldsymbol{k}_{||}\Delta\boldsymbol{r}_{||}} \quad (14)$$

As can be seen, Eq. (14) is equivalent to $G_{zz}(\boldsymbol{r},\boldsymbol{r'})$ given by equation (14) up to the sign, phase factor $e^{2ik_{1z}z'}(\approx 1$ for $z'=0)$ and a factor $\frac{k_{2z}}{k_{1z}}$ (which in our case is close to unity as shown in the next section). From here on we will suppose that $z'=0$ (as the thickness of antenna is very small), and $z=H$ is the height over the 2D-conductive layer, where we are calculating the field.

Approximation for the Dyadic Green's function

Let us define φ as the angle between the $k_{||}$ wavevector and the x-axis, so that $k_x = k_{||}cos\varphi, k_y = k_{||}sin\varphi, q = \frac{k_{||}}{k_0}$ and $\varepsilon = \frac{\varepsilon_1+\varepsilon_2}{2}$. Since in our case $\alpha_{x,y} = \frac{k_0 d\varepsilon_{x,y}}{2i} \ll 1$ and $k_{||} \gg k_0\sqrt{\varepsilon_i}$, the polaritons propagating along the layer are strongly confined and their wavelength is much smaller than the vacuum wavelength. Consequently, $k_{1z} \approx k_{2z} \approx ik_{||}$. Equation (13) can be thus simplified as:

$$G_{zz}(k_x,k_y) = \frac{-k_0\sqrt{\varepsilon_1\varepsilon_2}(\alpha_x sin^2\varphi+\alpha_y cos^2\varphi+iq)}{(\alpha_x sin^2\varphi+\alpha_y cos^2\varphi+iq)\left(\alpha_x cos^2\varphi+\alpha_y sin^2\varphi+\frac{\varepsilon_1+\varepsilon_2}{2iq}\right)-sin^2\varphi cos^2\varphi(\alpha_x-\alpha_y)^2} \quad (15)$$

Taking into account that $q \gg 1$, the Green's function can be further simplified:

$$G_{zz}(k_x,k_y) = \frac{-iqk_0\sqrt{\varepsilon_1\varepsilon_2}}{iq(\alpha_x cos^2\varphi+\alpha_y sin^2\varphi)+\varepsilon} \quad (16)$$

This function is related to DOS of hyperbolic polaritons propagating along the layer. The absolute value of $G_{zz}(k_x, k_y)$ is plotted in Fig. S1A as a function of k_x and k_y. It is still not possible to

calculate the Fourier transform from this expression explicitly. To simplify this expression, let us approximate the isofrequency curve (IFC) of polaritons, which is generally a quartic equation depending on the thickness of the layer and the permittivities of the different media *(36)*, by a hyperbola, $\frac{q_x^2}{\varepsilon_{y\,eff}} + \frac{q_y^2}{\varepsilon_{x\,eff}} = 1$. To that end, we match the asymptotes of the IFCs $\frac{q_x}{q_y} = \sqrt{-\frac{\varepsilon_y}{\varepsilon_x}}$ and the vertices of the hyperbola and the curve defined by zeroing the denominator of the expression (16): $q_x = \frac{2\varepsilon}{k_0 d\varepsilon_x}$, $q_y = 0$. As a result, we obtain expressions for $\varepsilon_{x\,eff} = \left(\frac{2\varepsilon}{k_0 d\sqrt{\varepsilon_x\varepsilon_y}}\right)^2$ and $\varepsilon_{y\,eff} = \left(\frac{2\varepsilon}{k_0 d\varepsilon_x}\right)^2$, and an expression for the Dyadic Green's function becomes integrable:

$$G_{zz}(k_x, k_y) = \frac{-2iq^2 k_0\sqrt{\varepsilon_1\varepsilon_2}}{k_0 d(\varepsilon_x q_x^2 + \varepsilon_y q_y^2) - \frac{4\varepsilon^2}{k_0 d\varepsilon_x}} \qquad (17)$$

Using equations (5) and (17), we obtain the expression for the Green's function in real space:

$$G_{zz}(\boldsymbol{r}, \boldsymbol{r}') \equiv G_{zz}(\boldsymbol{r} - \boldsymbol{r}') = \iint \frac{dq_x dq_y}{(2\pi)^2} \frac{q^2 k_0 e^{-qk_0 H} e^{ik_0\left(q_x(x-x') - q_y(y-y')\right)}}{k_0 d(\varepsilon_x q_x^2 + \varepsilon_y q_y^2) - \frac{4\varepsilon^2}{k_0 d\varepsilon_x}} \qquad (18)$$

We further assume that $\mathrm{Re}[\varepsilon_x] < 0$ and $\mathrm{Re}[\varepsilon_y] > 0$, which is the case of MoO_3 (in the parametric region of our interest), therefore, for each q_y the integrand (18) has a pole at some q_x, and the integral over q_x can be calculated using the Cauchy integral theorem and calculating residues:

$$G_{zz}(\boldsymbol{r} - \boldsymbol{r}') = \frac{i}{d}\int \frac{dq_y}{2\pi} \frac{\left(\frac{2\varepsilon}{k_0 d\varepsilon_x}\right)^2 - \frac{\varepsilon_y}{\varepsilon_x} q_y^2 + q_y^2}{2\varepsilon_x\sqrt{\left(\frac{2\varepsilon}{k_0 d\varepsilon_x}\right)^2 - \frac{\varepsilon_y}{\varepsilon_x} q_y^2}} e^{-qk_0 H} e^{ik_0\left(\Delta x\sqrt{\left(\frac{2\varepsilon}{k_0 d\varepsilon_x}\right)^2 - \frac{\varepsilon_y}{\varepsilon_x} q_y^2} - q_y \Delta y\right)} \qquad (19)$$

where $\Delta x = x - x'$, $\Delta y = y - y'$, and $q = \sqrt{\left(\frac{2\varepsilon}{k_0 d\varepsilon_x}\right)^2 - \frac{\varepsilon_y}{\varepsilon_x} q_y^2 + q_y^2}$.

The integral in expression (19) could be estimated by the stationary phase approximation, for this we expand the exponent power in a series up to the second order near the point with zero derivative, that is given by

$$q_y = \frac{-2\varepsilon\Delta y}{\sqrt{\varepsilon_y} k_0 d\sqrt{\varepsilon_x \Delta y^2 + \varepsilon_y \Delta x^2}} \qquad (20)$$

and

$$q = \frac{-2\varepsilon\sqrt{\varepsilon_x^2 \Delta y^2 + \varepsilon_y^2 \Delta x^2}}{\varepsilon_x\sqrt{\varepsilon_y} k_0 d\sqrt{\varepsilon_x \Delta y^2 + \varepsilon_y \Delta x^2}} \qquad (21)$$

Calculating the Gaussian integral, we obtain the DGF in the real space

$$G_{zz}(\boldsymbol{r}-\boldsymbol{r}') = \frac{\varepsilon^{\frac{3}{2}}}{\sqrt{\pi d}} \frac{\left(\varepsilon_x^2\Delta y^2+\varepsilon_y^2\Delta x^2\right)e^{-qk_0H}}{\varepsilon_x^2\varepsilon_y^{5/4}(k_0d)^2\left(\varepsilon_x\Delta y^2+\varepsilon_y\Delta x^2\right)^{5/4}} e^{i\left(\frac{2\varepsilon\sqrt{\varepsilon_x\Delta y^2+\varepsilon_y\Delta x^2}}{\varepsilon_x\sqrt{\varepsilon_y}d}-\frac{\pi}{4}\right)} \qquad (22)$$

where q is given by Eq. (21).

In Fig. S1A we plot the absolute value of $G_{zz}(\boldsymbol{r}-\boldsymbol{r}')$ (yellow dashed line), given by the expression (22), as a function of the polar angle at the distance r_0 (2.5 μm) from the dipole, and at the illuminating wavelength λ_0 =11.05 μm for a thickness d = 165 nm. Note that, according to the definition of the DGF, $G_{zz}(\boldsymbol{r}-\boldsymbol{r}')$, it represents the distribution of the z-component of the electric field emitted by a point electric dipole polarized along the z-direction. The polar distribution is superimposed on the color-plot plotted by Eq. 16, representing the hyperbolic IFC in the momentum space. The corresponding in-plane dielectric constants for α-MoO_3, taken from ref. *(22,35)*, are ε_{xx}=-4.13+0.34i and ε_{yy}=1.12+0.08i (see Section S5). Interestingly, we find that the near-field intensity shows a maximum DOS at an angle θ_c with respect to the [100] crystalline direction. As expected in hyperbolic media, such directions (yellow dashed lines in Fig. S1A) with maximum DOS are close to the asymptotes of the IFC (black dashed lines in Fig. S1A). Moreover, due to their large density, PhPs with high-$|\vec{k}|$ wavevectors (denoted by $\vec{k}_H$ in the main text) along such directions are dominant. Fig. S1B shows the full-wave simulation of the electric $|E_z|$ excited by a point electric dipole placed above the α-MoO_3 slab together with the polar distribution of the electric field in real space. As expected, the direction along which there is a maximum of the electric field intensity for PhPs with $\vec{k}_H$ coincides with the direction where a maximum $|E_z|$ appears in the numerical simulation.

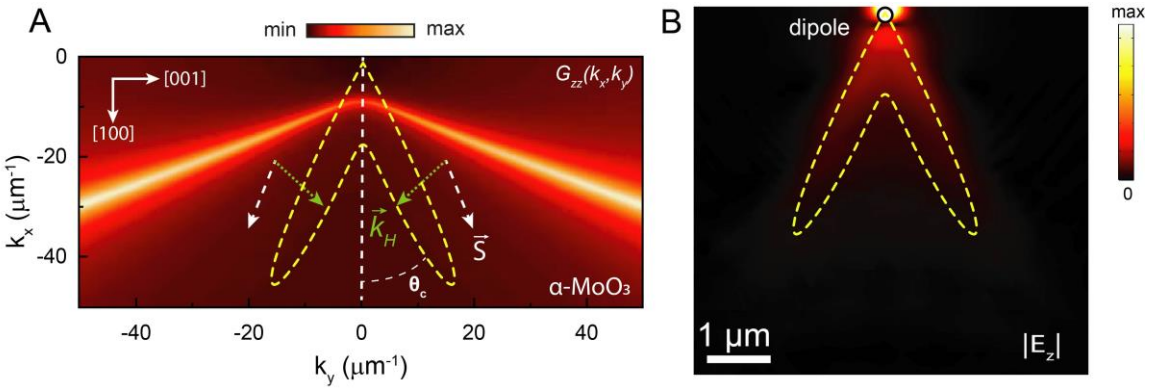

Fig. S1.- Calculation of the in-plane density of electromagnetic modes in α-MoO_3. (A) Color plot: Analytical calculation of the Green's function $G_{zz}(k_x,k_y)$ in momentum k-space, according to Eq. (16), for a 165-nm-thick α-MoO_3 slab at λ_0=11.05 μm. The polaritonic IFC contour is shown as maxima in the color plot. The yellow dashed line corresponds to the field intensity (absolute value of $G_{zz}(\boldsymbol{r}-\boldsymbol{r}')$) as a function of the polar angle at the distance r_0 from the dipole source. The white and green dashed arrows are the Poynting vector $\vec{S}$ and $\overrightarrow{k_H}$ wavevectors of PhPs propagating

along in-plane directions closely aligned with the asymptote of the hyperbolic IFC. The near-field intensity shows a maximum DOS at an angle θ_c with respect to the [100] crystal direction. The in-plane components of the α-MoO_3 dielectric permittivity are $\varepsilon_{xx} = -4.13 + 0.34i$ and $\varepsilon_{yy} = 1.12 + 0.08i$. **(B)** Numerical simulation of the electric $|E_z|$ (color plot) excited by a point electric dipole placed above the α-MoO_3 slab together with the polar distribution of the electric field in real space (yellow dashed lines) shown in (A).

Calculation of the field distribution around a metallic disk nanoantenna and the focal distance

As before, we will assume that the exciting electric field is polarized along the z-axis and deeply confined to the disk edge. This assumption mimics the excitation by a metal disk nanoantenna placed on an α-MoO_3 slab (approximated by a 2D layer). Hence, the electric field at any point (x, y) is given by Eq. (1) and the z-component of this field reads:

$$E_z(x,y) = k_0^2 \int dx'dy' G_{zz}(x-x', y-y') E_0 dR\delta(x' - \sqrt{R^2 - y'^2}) \qquad (23)$$

where $\delta(x)$ is the Dirac delta function and R is the radius of the disk. By changing to polar coordinates $(x', y') \rightarrow (r', \theta)$ we obtain:

$$E_z(x,y) = \frac{E_0 R^2 \varepsilon^{\frac{3}{2}}}{\varepsilon_x^2 \varepsilon_y^{5/4} d} \int d\theta \frac{\left(\varepsilon_x^2 (y - R\sin\theta)^2 + \varepsilon_y^2 (x - R\cos\theta)^2\right) e^{-qk_0 H}}{\sqrt{\pi d}\left(\varepsilon_x (y - R\sin\theta)^2 + \varepsilon_y (x - R\cos\theta)^2\right)^{5/4}} e^{i\left(\frac{2\varepsilon\sqrt{\varepsilon_x (y - R\sin\theta)^2 + \varepsilon_y (x - R\cos\theta)^2}}{\varepsilon_x \sqrt{\varepsilon_y} d} - \frac{\pi}{4}\right)} \quad (24)$$

where

$$q = \frac{-2\varepsilon\sqrt{\varepsilon_x^2 (y - R\sin\theta)^2 + \varepsilon_y^2 (x - R\cos\theta)^2}}{\varepsilon_x \sqrt{\varepsilon_y} k_0 d \sqrt{\varepsilon_x (y - R\sin\theta)^2 + \varepsilon_y (x - R\cos\theta)^2}} \qquad (25)$$

Equation (24) approximates the total electric field at the point (x, y, H) created by polaritons excited from the edge of the disk. The integral in (24) adds the contribution of point-like electric dipoles located along the disk edge at points (x', y') with radius-vectors forming an angle θ with the x-axis ([100] crystal direction of α-MoO_3). From equation (24), using stationary phase approximation, we calculate the field distribution along the x-axis:

$$E_z(x,y) = E_0 \frac{2\varepsilon R^3}{\varepsilon_x \varepsilon_y d} \sqrt{\frac{\varepsilon_x}{\varepsilon_x - \varepsilon_y}} \frac{1}{R^2 - \frac{\varepsilon_y}{\varepsilon_y - \varepsilon_x} x^2} \exp\left(i \frac{2\varepsilon\sqrt{R^2 - \frac{\varepsilon_y}{\varepsilon_y - \varepsilon_x} x^2}}{d\sqrt{\varepsilon_x \varepsilon_y}} + \frac{2\varepsilon RH}{d\sqrt{\varepsilon_x \varepsilon_y}\sqrt{R^2 - \frac{\varepsilon_y}{\varepsilon_y - \varepsilon_x} x^2}} \right) \quad (26)$$

Using Eq. (24), we immediately obtain the following expression for the position of the focus (focal distance x_f) with respect to the edge of the disk:

$$x_f \approx R\sqrt{1 - \frac{\varepsilon_x'}{\varepsilon_y'}} \qquad (27)$$

where $\varepsilon'_{x,y}$ is the real part of the complex-valued dielectric function $\varepsilon_{x,y}$.

Calculation of the focal distance for rod-like trapezoidal nanoantennas

The geometry of the rod-like trapezoidal nanoantennas (see Fig. 3 of the main manuscript) has been optimized (see section S3) to avoid scattering and/or absorption of the excited polaritons with the edges of the antennas, thus enhancing the near-field intensity at the focal spot marked with a dashed red circle in Fig. S2. For this, the angle between the x-axis and the edges of the antenna should be bigger than the angle between the x-axis and the direction along which the radiation intensity is maximum, so that the relationship $\frac{y_2-y_1}{x_1} > \mathrm{Re}[\tan(\theta_c)] \approx \sqrt{-\frac{\varepsilon'_y}{\varepsilon'_x}}$ is fulfilled. The focal spot is therefore formed exactly at the intersection of the rays coming from the extreme points of the antenna edges, at the point with coordinates $(x_f, 0)$, as shown in Fig. S2, and with x_f given by:

$$x_f \approx \frac{1}{2}\left(x_1 + y_1\sqrt{-\frac{\varepsilon'_x}{\varepsilon'_y}} + x_2 + y_2\sqrt{-\frac{\varepsilon'_x}{\varepsilon'_y}}\right) \approx \frac{x_1}{2} + \frac{y_1+y_2}{2}\sqrt{-\frac{\varepsilon'_x}{\varepsilon'_y}} \qquad (28)$$

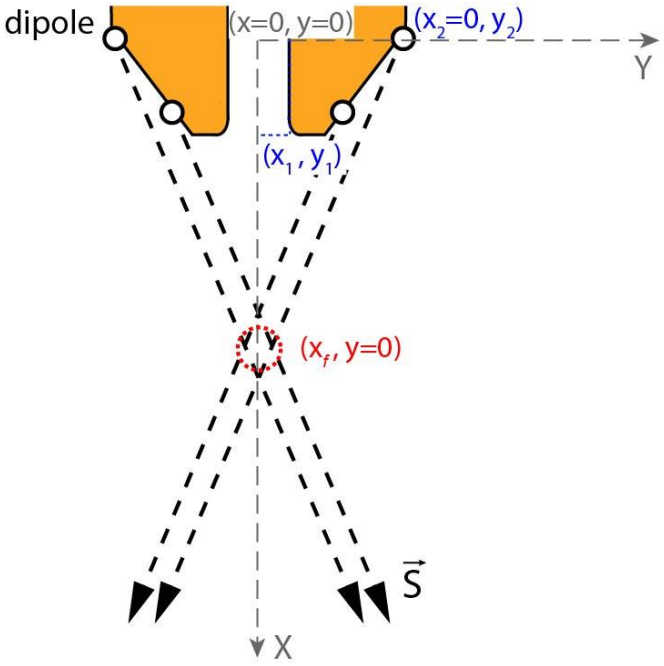

Fig. S2.- Understanding the focusing of in-plane PhPs in α-MoO_3 employing rod-like trapezoidal nanoantennas. Focusing of PhPs excited by four electric point dipoles placed along the sidewall of rod-like trapezoidal nanoantennas on an α-MoO_3 slab. The black dashed arrows represent the Poynting vector of polaritons with wavevectors $\overrightarrow{k_H}$. The interference of polaritons gives rise to a focal spot marked by a red dashed circle. The x-axis and y-axis correspond to the [100] and [001] crystalline directions in α-MoO_3, respectively.

S2. Demonstration of the negligible contribution of low-$\vec{k}$ hyperbolic PhPs to the formation of a focal spot.

Fig. S3A shows the simulated near-field distribution, Re(E_z), excited by an Au disk-like nanoantenna on a 165-nm-thick α-MoO_3 slab (λ_0=10.85 μm). As mentioned in the main manuscript, we obtain a convex wavefront confined within a triangular region in which a focusing spot is formed at its apex due to the interference of PhPs with $\vec{k}_H$. Additionally, a concave wavefront is found centred along the [100] crystalline direction, attributed to propagating PhPs with low-$\vec{k}$ wavevectors (within the sector defined by the IFC asymptotes).

To unambiguously verify that the formation of the convex interference fringes (including the focal spot) is due to a major contribution of PhPs with $\vec{k}_H$, while the contribution of polaritons with low-$\vec{k}$ wavevectors is minor, we plot a profile of the near-field image along the [100] direction (black dashed line) and analyze the periodicity of the convex interference fringes in Fig. S3B. In agreement with our claims, a shorter periodicity is found for the convex wavefronts (green colored area, $\lambda_{fringes}$ ~ 540 nm), in comparison with the concave wavefronts (pink colored area, λ_p ~ 610 nm), the latter being the characteristic wavelength for propagating low-$\vec{k}$ PhPs in α-MoO_3 along the [100] direction *(22,35)*.

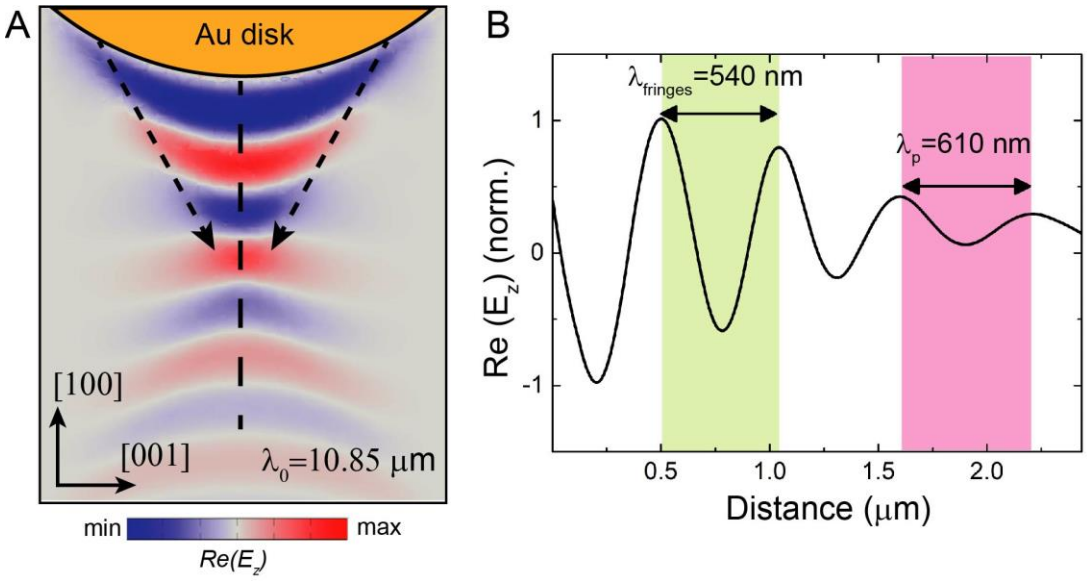

Fig. S3.- Focusing of in-plane PhPs in α-MoO_3 employing a Au disk nanoantenna. (A) Simulated near-field image, *Real(E_z)*, on an Au disk nanoantenna fabricated on a 165-nm-thick α-MoO_3 slab under illumination at λ_0=10.85 μm. **(B)** Profile along the dashed black line marked in (a). The convex fringes attributed to the interference of PhPs with $\vec{k}_H$ present a periodicity $\lambda_{fringes}$=540 nm (green area), whereas concave fringes attributed to propagating low-$\vec{k}$ PhPs show a characteristic polariton's wavelength λ_p=610 nm along the [100] direction (pink area).

S3. Optimizing the geometry of rod-like trapezoidal nanoantennas for an enhanced PhPs focusing.

As discussed in sections S1 and S2, the focal spot is due to the interference of PhPs with $\vec{k}_H$ wavevectors propagating on the surface of the α-MoO_3 slab along a direction closely aligned with the asymptotes of the IFC. To maximize the near-field intensity at the focus position, we designed rod-like trapezoidal nanoantennas with flat extremities that form an angle θ_{ant} with respect to the [100] crystalline direction (Fig. S4). This angle is optimized for an illuminating wavelength λ_0=11.05 μm with the use of full-wave numerical simulations. This geometry favors both an increase of the density of PhPs with high-$\vec{k}$ wavevectors excited from the contour of the antenna's flat edge at the focal spot and a null contribution of PhPs with low-$\vec{k}$ wavevectors. In particular, we calculate the total power dissipation inside a 165-nm-thick α-MoO_3 slab in a cylindrical volume (circular base with diameter ~225 nm – FWHM value of the focal spot – and height equal to the slab's thickness ~165 nm, shadowed green area in Fig. S4A-C) and the total electric field $|E|^2$ above the surface of the slab in a cylindrical volume (circular base with diameter ~225 nm – FWHM value of the focal spot – and height ~80 nm, shadowed green area in Fig. S4a-c). The result as a function of the angle θ_{ant} of the trapezoidal rod-like nanoantennas is shown in Fig. S4D. We find an optimal value of θ_{ant} ~44º, for which both the power dissipation and the electric field intensity are clearly enhanced. This angle is the one used for the fabrication of the rod-like trapezoidal antennas shown in this work.

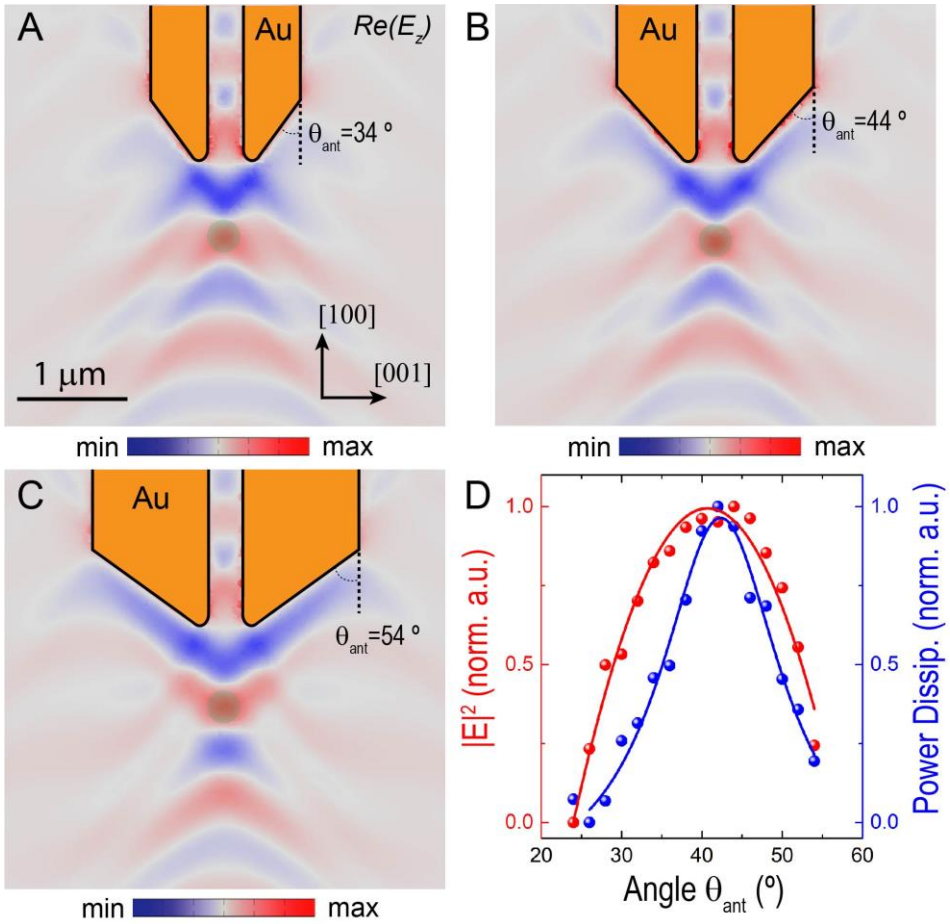

Fig. S4.- Optimization of the extremities of rod-like trapezoidal Au nanoantennas. (A-C) Simulated, *Re(Ez)*, near-field image on Au rod-like trapezoidal nanoantennas fabricated on a 165-nm-thick α-MoO_3 slab at λ_0=11.05 μm for angles θ_{ant}= 34º, 44º and 54º. **(D)** Normalized integrated field intensity, $|E|^2$, (red dots) above the slab and power dissipation density (blue dots) within the slab in a cylindrical volume at the focal spot (shadowed green area in a-c) as a function of the angle θ_{ant} between the [100] crystalline direction and nanoantennas' edge.

S4. Tunability of the focal distance *f* by varying the distance between rod-like trapezoidal nanoantennas

As discussed in the main manuscript, the focal distance can be tuned by varying the incident wavelength λ_0. Alternatively, it can be also changed by varying the distance between the individual rod-like trapezoidal nanoantennas *d*. The simulated near-field images in Fig. S5 show that the focal distance can be tuned from ~ 770 nm to ~1050 nm when the *d* varies from 320 nm to 620 nm, respectively. A slope angle θ_{ant}= 44º is used in the design of the antennas based on our findings presented in section S3.

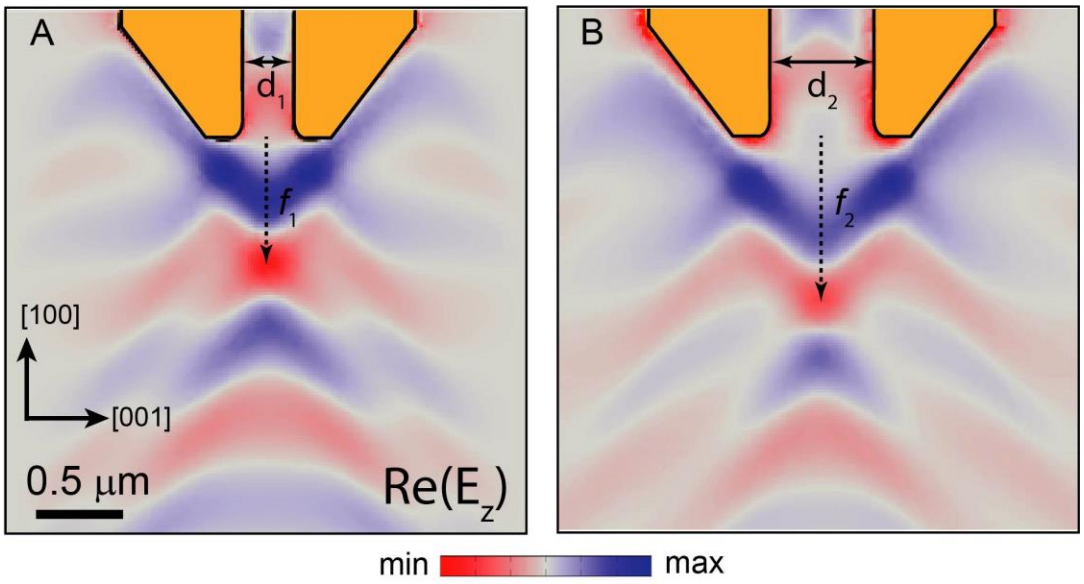

Fig. S5.- Tuning of the focal distance employing rod-like trapezoidal Au nanoantennas. Simulated real-space field distribution, *Re(E_z)*, on rod-like trapezoidal nanoantennas' extremities (λ_0=11.05 μm) for different separation distances *d* between them: **(A)** d_1=320 nm and **(B)** d_2=620 nm. The focal distance can be tuned by varying the nanoantennas separation from f_1=770 nm in (a) to f_2= 1050 nm in (b). The sidewalls of the nanoantenna at both extremities present an angle of about 44º with respect to the [100] direction.

S5. Dielectric permittivity of α-MoO_3 and SiO_2

The dielectric function of α-MoO_3 is obtained from correlative far- and near-field measurements, as reported in *(35)*, while the real part of the dielectric function of SiO_2 used throughout the work is adjusted by comparing the experimental dispersion of PhPs propagating in α-MoO_3 slabs on top of SiO_2 with that obtained from analytical and transfer-matrix calculations, and full-wave numerical simulations. In particular, the analytical dispersion of propagating PhPs in α-MoO_3 slabs with thickness d on SiO_2 substrates is given by *(36)*:

$$k = \frac{\rho}{d}\left[\arctan\left(\frac{\rho\varepsilon_1}{\varepsilon_z}\right) + \arctan\left(\frac{\rho\varepsilon_2}{\varepsilon_z}\right) + \pi l\right], \qquad l = 0, 1, 2 \ldots, \tag{29}$$

where k is the in-plane component of the wavevector, with $k^2 = k_x^2 + k_y^2$, $\rho = i\sqrt{\varepsilon_z/(\varepsilon_x \cos^2\alpha + \varepsilon_y \sin^2\alpha)}$, being α the angle between the x axis and $\boldsymbol{k}$. ε_1 and ε_2 are the permittivities of the air superstrate ($\varepsilon_1 = 1$) and SiO_2 substrate, respectively, and l is the mode index.

The real part of the permittivity value of SiO_2 is adjusted by comparing the experimental PhPs dispersion obtained by scattering-type scanning near-field optical microscopy (s-SNOM) measurements on α-MoO_3/SiO_2 along the [100] crystalline direction of α-MoO_3 with that obtained from the analytical dispersion from Eq. (27) and transfer-matrix calculations *(37)*, in which the imaginary part of the Fresnel reflection coefficient of the system, $\mathrm{Im}[r_p(k,\omega)]$ is computed, being

ω the incident frequency. As shown in Fig. S6, we find a perfect agreement between the calculated analytical dispersion (dashed red lines), transfer-matrix calculations (false color plot), and the values extracted from numerical simulations (black dots) and s-SNOM measurements (white dots) in α-MoO_3 slabs with different thicknesses, namely 166 nm, 142 nm, and 250 nm. We highlight that the successful fitting of the polaritonic response in α-MoO_3 flakes with different thicknesses further validates the obtained dielectric function values for the SiO_2 substrate, especially considering the strong thickness dependence of hyperbolic polaritons. We also note that we neglected the optical losses in the SiO_2 substrate. The resulting real part of the dielectric permittivity of SiO_2 for the whole wavelength range of interest is shown in Fig. S7 *(38)*.

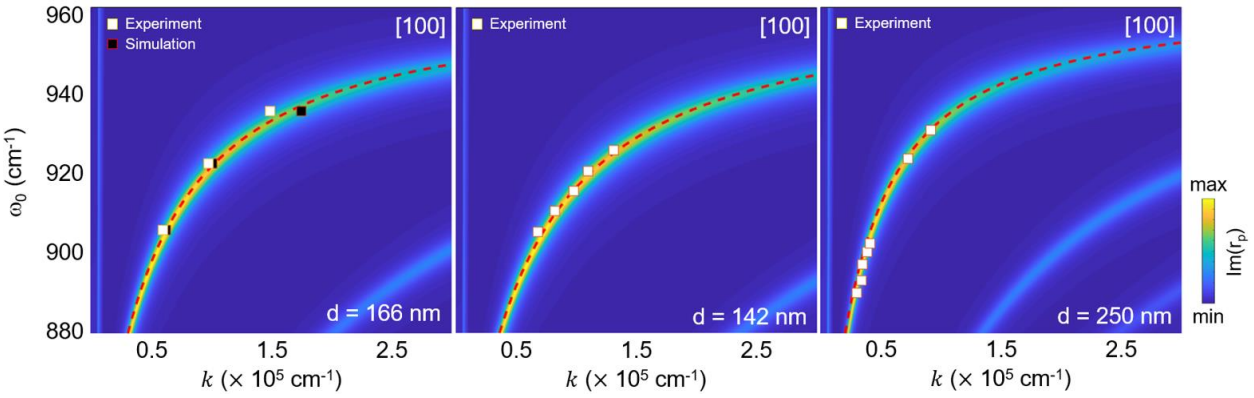

Fig. S6.- Comparison between experimental/theoretical dispersion curves of in-plane PhPs in α-MoO_3 on SiO_2 substrates. False color plot of the imaginary part of the Fresnel reflection coefficient, $Im[r_p(k,\omega)]$, together with the calculated analytical dispersion from Eq. (1) (dashed red lines) and values extracted from s-SNOM measurements (white dots) and full-wave numerical simulations (black dots), for α-MoO_3 flakes of different thicknesses: 166 nm, 142 nm, and 250 nm.

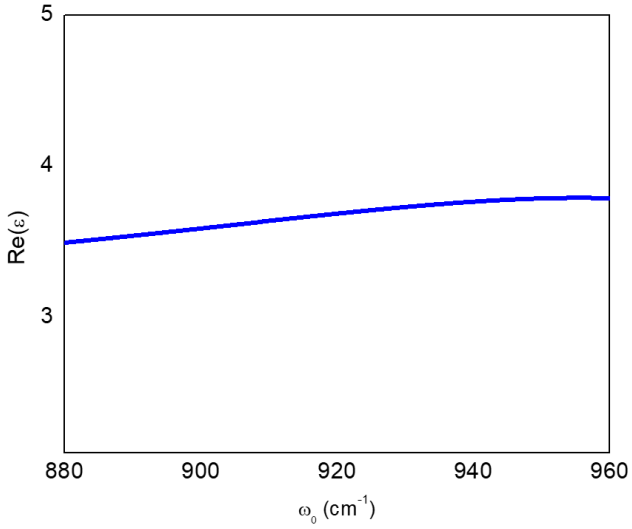

Fig. S7.- Infrared dielectric permittivity of SiO_2. Real-part of the infrared dielectric permittivity of SiO_2 used in this work.

S6. Comparison of PhPs launched by an Au disk-like nanoantenna in in-plane isotropic and in-plane hyperbolic media.

Fig. S8 shows the near-field full-wave numerical simulations of PhPs launched by a disk-like Au nanoantenna on a 165-nm-thick α-MoO_3 slab with in-plane hyperbolicity (Fig. S8A, with ε_{xx} = -4.13+0.34i; ε_{yy} = 1.12+0.08i; ε_{zz} = 9.04+0.06i) and an in-plane isotropic medium (Fig. S8B, with $\varepsilon_{xx}=\varepsilon_{yy}$=-4.13+0.34i; ε_{zz} = 9.04+0.06i) at an illuminating wavelength λ_0=11.05 μm. In the in-plane isotropic medium, PhPs propagate in all in-plane directions (***k*** wavevectors and Poynting vectors ***S*** are collinear) leading to a circular wavefront parallel to the nanoantenna's edges (Fig. S8B). In stark contrast, highly anisotropic propagation of PhPs with concave wavefronts is obtained in in-plane hyperbolic α-MoO_3 (Fig. S8A), where ***k*** wavevectors and Poynting vectors ***S*** are generally not collinear. Highly directional PhPs in α-MoO_3 with Poynting vector $\vec{S}$ and wavevectors ($\vec{k}_H$) closely aligned along the asymptote of the IFC (see Fig. 1A in the main text), are depicted in Fig. S8A with black and green dashed arrows, respectively.

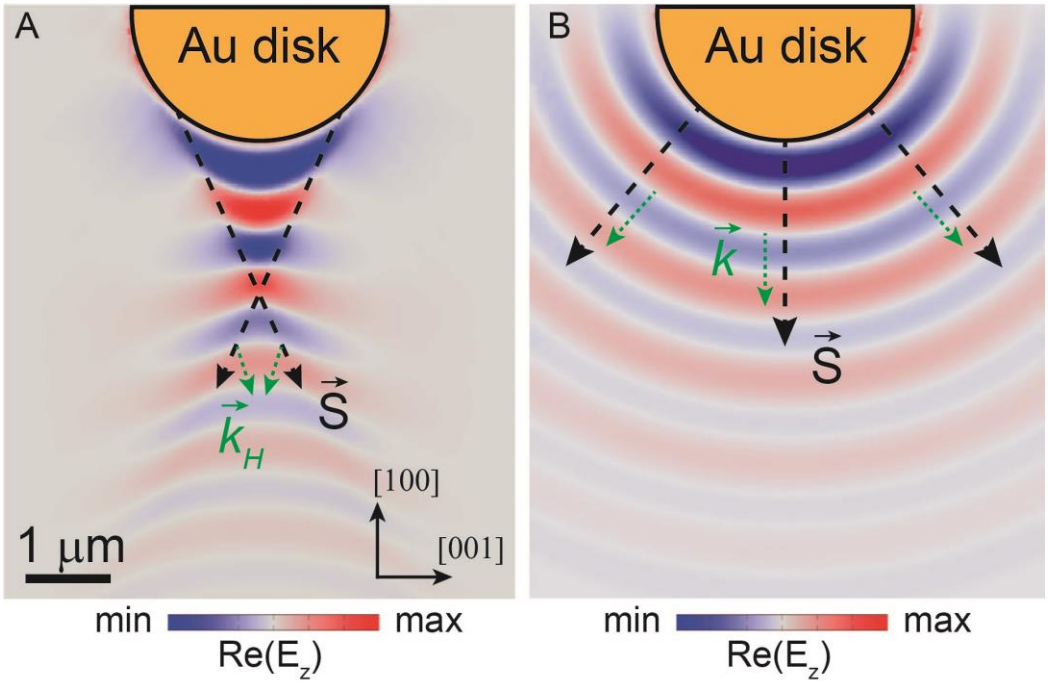

Fig. S8.- Propagation of PhPs launched by a Au disk nanoantenna along the surface of in-plane hyperbolic and isotropic media. Simulated near-field distribution, *Re(E_z)*, on disk-like Au nanoantennas at incident wavelength λ_0=11.05 μm in **(A)** in-plane hyperbolic α-MoO_3 medium, and **(B)** in-plane isotropic medium.

S7. Understanding the focusing of in-plane hyperbolic PhPs using disk-like nanoantennas in hyperbolic α-MoO_3

As mentioned in the main text of the manuscript, the in-plane focusing of PhPs in a hyperbolic medium (α-MoO_3) by employing a disk-like Au nanoantenna can be understood by considering the Huygens' principle. In this regard, the nanoantenna with in-plane circular geometry can be seen as an extended source composed by an infinite number of point-like dipoles situated along its edge. Such dipoles launch PhPs in the hyperbolic medium and their wavefronts interfere. The resulting near-field interference pattern exhibits convex fringes with large near-field amplitude within a triangular region, and a focusing spot is formed at its apex (yellow dashed circle in Fig. S9).

To find out the origin of such interference pattern, we perform full-wave numerical simulations where a discrete number of point electric dipoles, situated on an α-MoO_3 slab along part of a semicircle, thus mimicking the nanoantenna's periphery, are used for the excitation of PhPs. In a first approximation, we only consider the bottom part of the nanoantenna from where PhPs can be excited by placing point dipoles along its contour. As it can be seen in Fig. S9A-C, the near-field distribution observed when a disk-like nanoantenna is employed can be well reproduced by considering the interference of highly directional PhPs excited by the point dipoles with Poynting vector $\vec{S}$ (black dashed arrows), and wavenumbers $\vec{k}_H$ (green dashed arrows) closely aligned along the asymptote of the IFC (see Fig. 1A in the main text). We note that increasing the number of point electric dipoles along the semicircle mimicking the half nanoantenna's edge does not introduce noticeable differences in the interference pattern, as shown in Fig. S9C and Fig. S10. Hence, a negligible contribution of PhPs stemming from distant regions at the edges of the nanoantenna can be concluded.

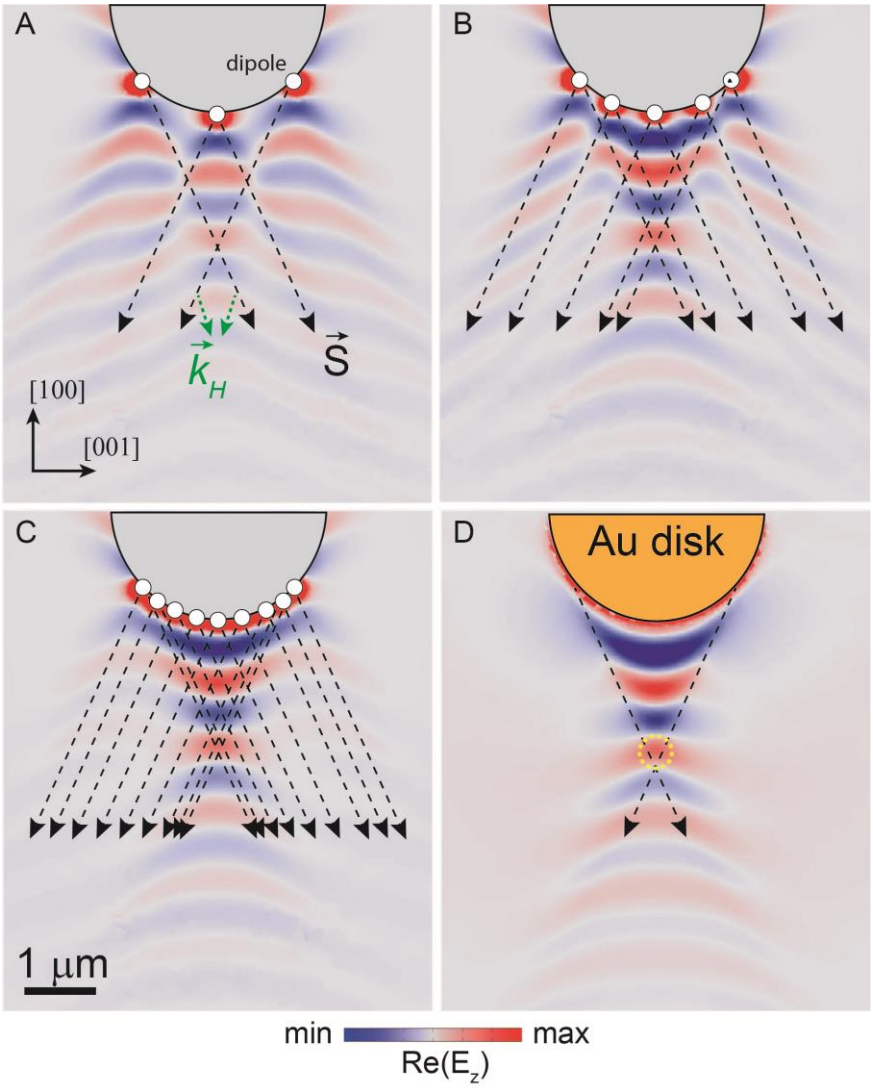

Fig. S9.- Focusing of in-plane PhPs in α-MoO_3 employing Au disk nanoantennas. (A-C) Full-wave numerical simulations of the near-field distribution, *Re(E_z)*, for a varying number of point electric dipoles (launchers of in-plane PhPs) situated above a 165-nm-thick α-MoO_3 slab's surface, and along a circle that mimics the in-plane circular periphery of a disk-like Au nanoantenna. **(D)** Same as (a) for the case where a disk-like Au nanoantenna is employed for the excitation of the PhPs where a focal spot is marked with a yellow dashed line. An incident wavelength λ_0=11.05 μm is used in both cases.

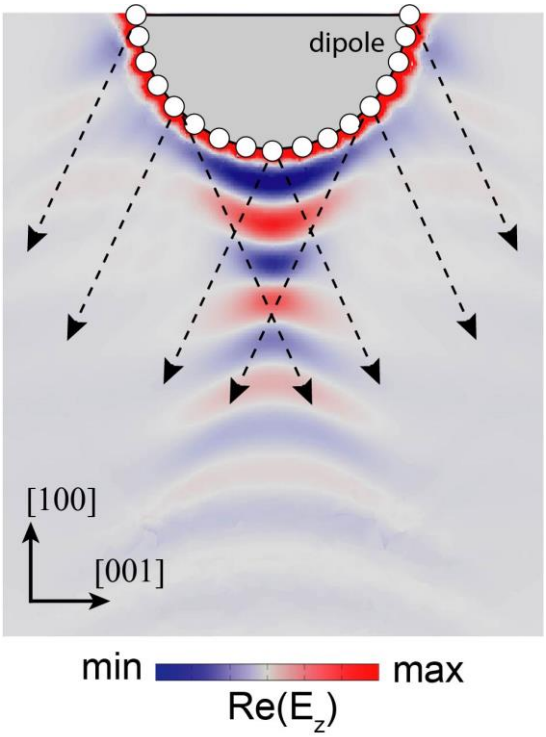

Fig. S10.- Modelling the focusing of in-plane PhPs in α-MoO_3 by employing a discrete distribution of point dipoles. Full-wave numerical simulations of the near-field distribution, *Re(E_z)*, for a distribution of point electric dipoles (launchers of in-plane PhPs) situated above a 165-nm-thick α-MoO_3 slab's surface, and along a semicircle that mimics the in-plane circular periphery of a disk-like Au nanoantenna. An incident wavelength λ_0=11.05 μm is used.

S8. Optimizing metal rod-like nanoatennas with concave extremities for the focusing of PhPs in in-plane isotropic media.

The optimal nanoantenna's geometry for the excitation and focusing of PhPs in an in-plane isotropic medium is given by a rod-like antenna with a concave circular geometry at its extremity. The concave shape is justified by considering that the incident wavelength (11.05 μm) is much larger than the lateral dimensions of the metal antenna (~ 3 μm). Therefore, following the Huygen's principle, the PhPs launched at the antenna's extremity are all in phase and interfere constructively as they propagate yielding an overall circular wavefront. Hence, the ideal shape of the antenna's extremity must be circular to ensure that the excited PhPs are interfering constructively at the focal spot ensuring a minimal FWHM value.

On the other hand, the radius of the circular shape of the antenna's extremity is optimized as shown in Fig. S11, where full-wave numerical simulations of the near-field, *Re(E_z)*, on rod-like nanoantennas with a concave circular extremity of varying radius are depicted. As it can be seen, no clear and well-defined focal spot is obtained for a radius value below ~0.6 μm. The optimal radius value is found to be ~1 μm so that a minimal FWHM value of the focal spot is obtained as shown in Fig. S12. Additionally, we note that obtained focal distance (~0.9 μm) is the shortest

possible thus ensuring a minimum damping in the propagation of the interfering PhPs at the focal spot.

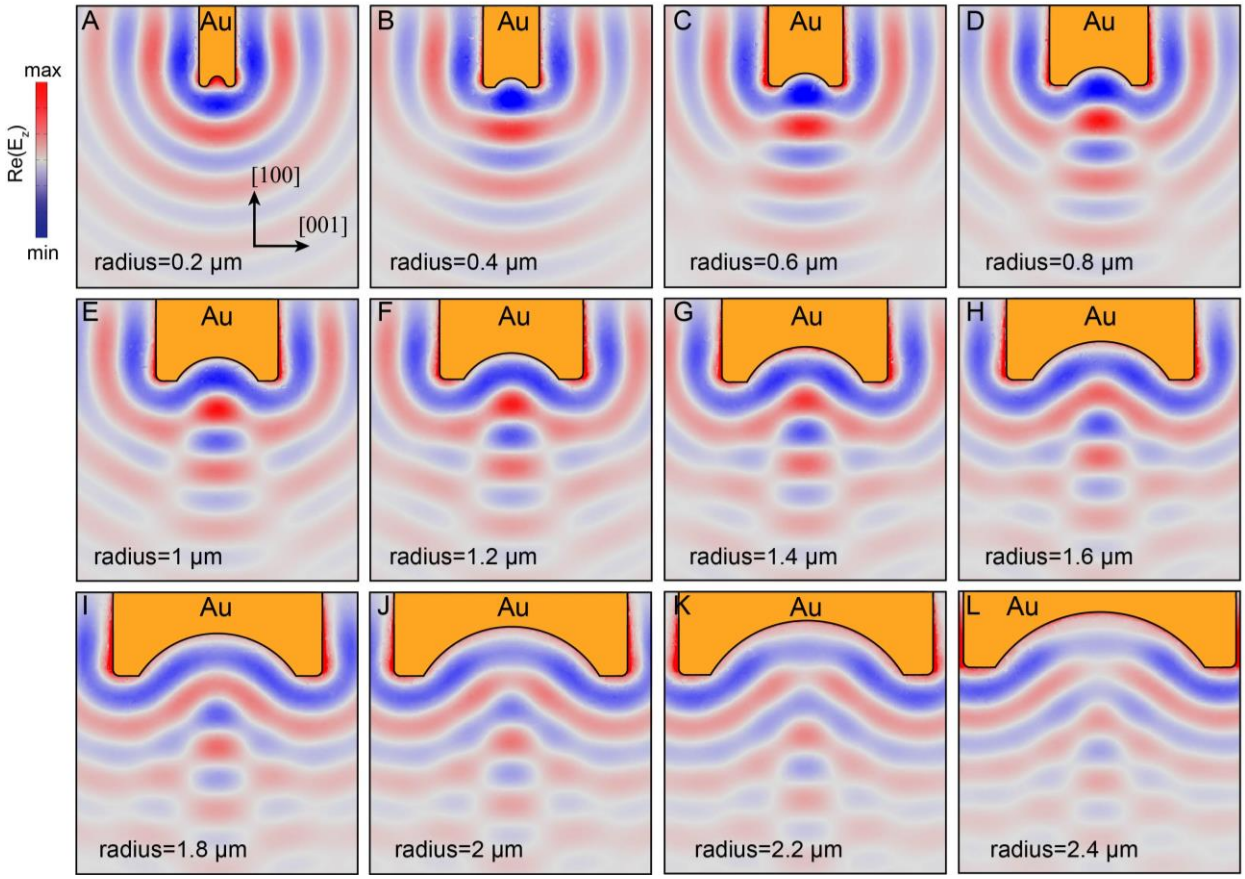

Fig. S11.- Optimization of rod-like Au nanoantennas to focus PhPs in in-plane isotropic media. Full-wave numerical simulations of the near-field distribution, *Re(E_z)*, for a rod-like Au nanoantenna with a concave circular extremity on top of a 165-nm-thick slab. The radius of the circular extremity is varied: **(A)** 0.2 μm; **(B)** 0.4 μm; **(C)** 0.6 μm; **(D)** 0.8 μm; **(E)** 1 μm; **(F)** 1.2 μm; **(G)** 1.4 μm; **(H)** 1.6 μm; **(I)** 1.8 μm; **(J)** 2 μm; **(K)** 2.2 μm; **(L)** 2.4 μm. The profiles along the dashed lines in (A-H) are shown in Fig. S12.

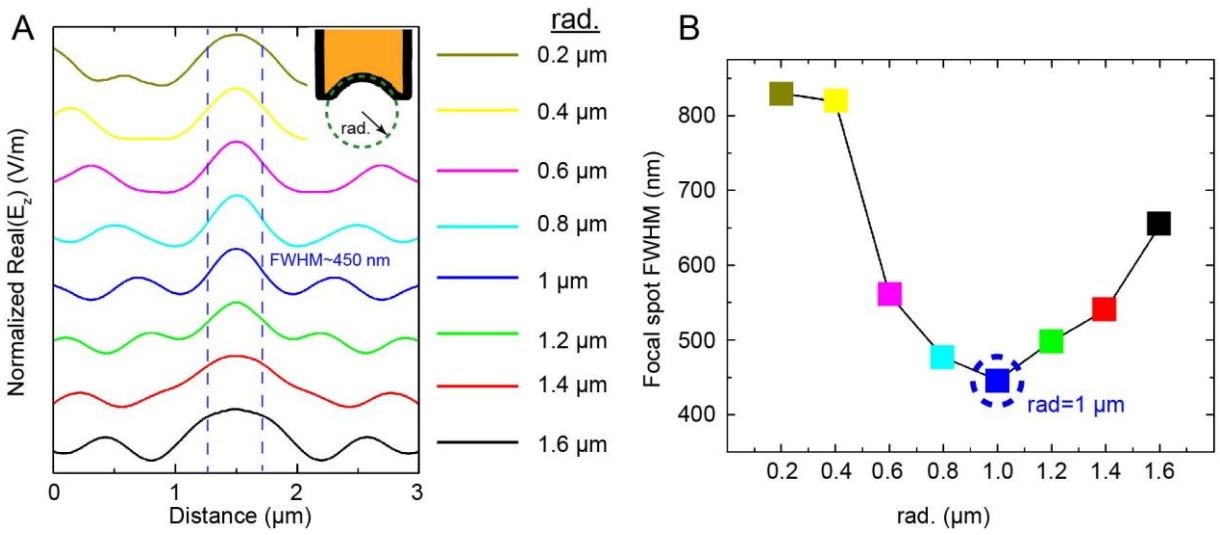

Fig. S12.- Optimization of the concave extremity's curvature in rod-like Au nanoantennas in in-plane isotropic media. (A) Near-field profiles, *Re(E_z)*, along the dashed lines marked on the full-wave numerical simulations shown in Fig. S11. The profiles are shown for several radius values of the circular concave extremity of the rod-like nanoantenna. **(B)** FWHM values of the focal spots identified on each of the profiles shown in (A). A minimum FWHM value is found for a radius value of 1 μm.

S9. Propagation of in-plane hyperbolic PhPs in α-MoO_3.

The in-plane hyperbolic IFC - a slice of the polariton dispersion in the momentum-frequency space defined by a plane of constant frequency (ω) – for PhPs in a α-MoO_3 slab at infrared frequencies (illuminating wavelength λ_0=11.05 μm) is shown in Fig. S13A. According to this IFC, the propagation of PhPs in α-MoO_3 is only allowed along specific directions laying within the sectors $|\tan(k_x/k_y)| < \sqrt{-\varepsilon_y/\varepsilon_x}$ between the asymptotes of the hyperbola in the (k_x, k_y) space (x and y corresponding to the α-MoO_3 [001] and [100] crystalline directions, respectively). Furthermore, the Poynting vector $\vec{S}$, which determines the propagation direction of PhPs in real space and is perpendicular to the IFC, is generally non-collinear with the wavevector $\vec{k}$. This is in stark contrast to the propagation of waves in in-plane isotropic media where $\vec{S}$ and $\vec{k}$ are collinear, and thus leads to exotic and non-intuitive optical phenomena. Remarkably, when approaching the two asymptotes of the IFC, the number of available wavevectors of PhPs largely increases (high-$|\vec{k}|$ wavevectors, denoted by $\vec{k}_H$), which yields a highly directional ray-like propagation as shown in Fig. S13A. Additionally, the latter leads to the existence of concave wavefronts centered along the y-axis, as demonstrated in Fig. S13B, where the real part of the full-wave simulated near-field distribution, $Re(E_z(x,y))$, of a vertical point dipole in close proximity to α-MoO_3 is represented (PhPs with $\vec{k}_H$ wavevectors are marked with black dashed arrows). For comparison, the case of PhPs propagating in a conventional in-plane isotropic medium is shown in the inset to Fig. S13B, where divergent PhPs propagation with convex wavefronts is instead observed.

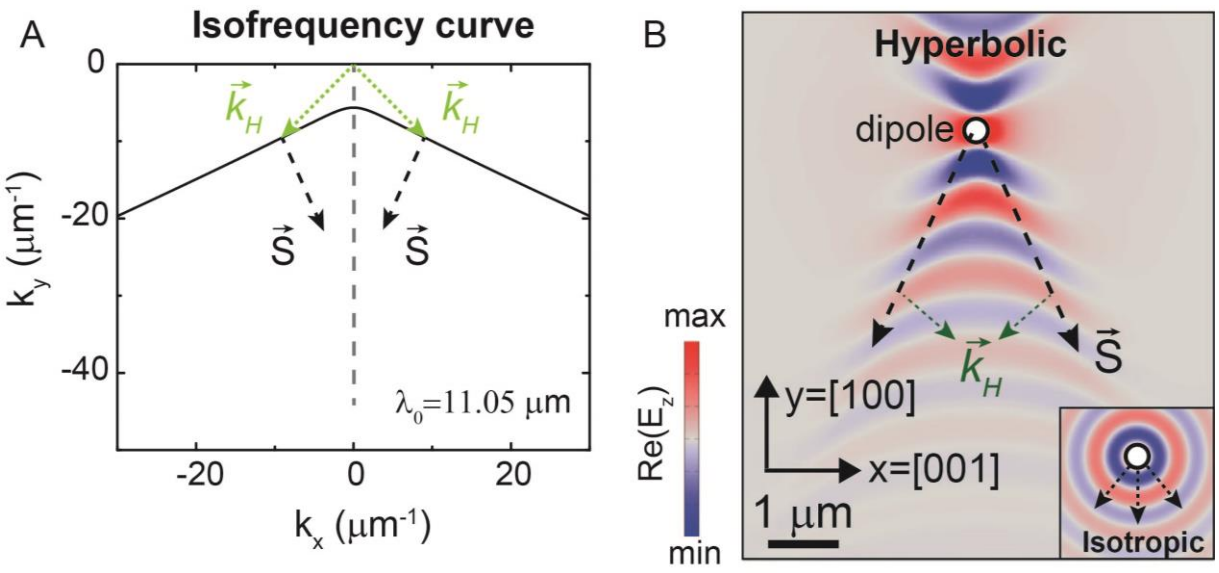

Fig. S13.- In-plane propagation of PhPs in α-MoO_3. (A) IFC of in-plane hyperbolic PhPs in a 165-nm-thick α-MoO_3 crystal at an illuminating wavelength λ_0=11.05 μm. PhPs with high-$|\vec{k}|$ wavevectors propagating closely along the asymptote of the hyperbola are indicated by $\vec{k}_H$, together with their Poynting vector $\vec{S}$. **(B)** Simulated real part of the near-field distribution, *Re(Ez)*, of propagating PhPs excited by a vertically-oriented electric point dipole situated over the surface of the α-MoO_3 crystal. The inset shows the case for an in-plane isotropic medium.

S10. Hyperbolic in-plane PhPs focusing in α-MoO_3 employing rod-like trapezoidal metal nanoantennas: electric field profiles, Re(σ_3), along [100] and [001] crystalline directions at the focus.

Fig. S14A shows the experimental near-field image, *Re(σ_3)*, on rod-like trapezoidal Au nanoantennas on a 165-nm-thick α-MoO_3. A deep-subwavelength focal spot with a FWHM value of 225 nm is obtained upon the interference of in-plane high-$\vec{k}$ polaritons. The profiles along both [001] and [100] in-plane crystalline directions at the focal spot are depicted in Fig. S14B. A similar FWHM value is obtained along both directions.

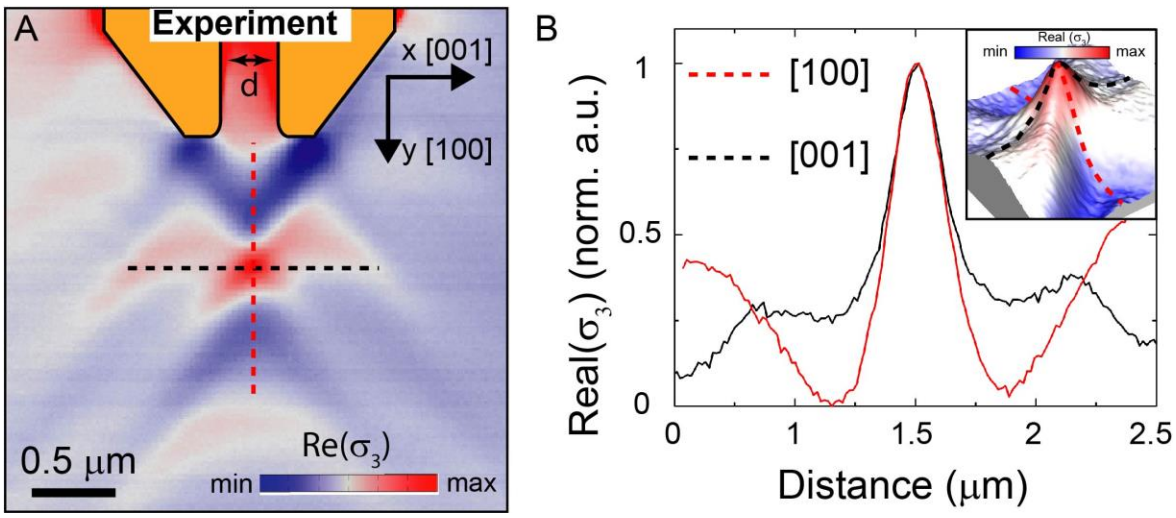

Fig. S14.- Focal spot dimensions along [100] and [001] orthogonal directions in α-MoO_3. (A) Experimental near-field image, *Re(σ_3)*, of rod-like trapezoidal nanoantennas (*d*=320 nm) on a 165-nm-thick α-MoO_3 slab for an illuminating wavelength λ_0=11.05 μm. **(B)** Profiles on the near-field image in (A) along the crystalline directions [100] (red dashed line in (A)) and [001] (black dashed line in (A)). The inset shows a 3D plot of the focal spot in (A).

S11. Optimizing the length of resonant metal Au nanoantennas.

Fig. S15A and S15B show the normalized near-field intensity, $|E_z|$, on top of a rod-like trapezoidal nanoantenna (the antenna is placed on a in-plane hyperbolic α-MoO_3 slab oriented along the [100] crystalline direction in α-MoO_3) and a rod-like nanoantenna with a concave circular extremity (the antenna is placed on a in-plane isotropic slab), respectively, as a function of the rod nanoantennas' length. The thickness of the slabs is set to 165 nm. A resonant rod's length value of L~3 μm and L~3.2 μm is found for the rod-like trapezoidal nanoantenna and the rod-like nanoantenna with a concave circular extremity, respectively.

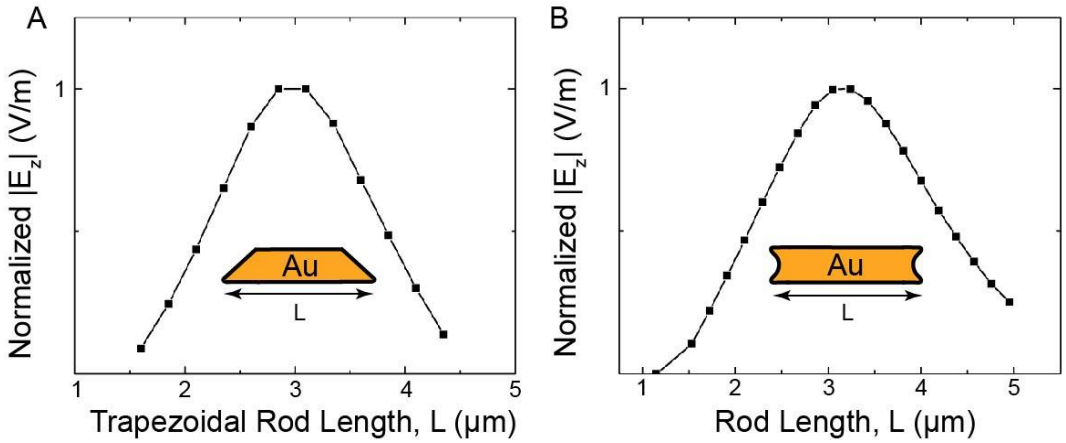

Fig. S15.- Optimization of the length of rod-like nanoantennas. (A) Normalized near-field intensity, $|E_z|$, as a function of the length of a rod-like trapezoidal nanoantenna (L) on a 165-nm-

thick in-plane hyperbolic α-MoO_3 slab for an illuminating wavelength λ_0=11.05 μm (ε_{xx}=-4.1323+0.3456i; ε_{yy}=1.1205+0.0814i; ε_{zz}=9.045+0.0644i). The resonance is found for a value L~3 μm. **(B)** Normalized near-field intensity, $|E_z|$, as a function of the length of a rod-like nanoantenna with a concave circular extremity on a 165-nm-thick in-plane isotropic slab for an illuminating wavelength λ_0=11.05 μm (ε_{xx}=ε_{yy}=-4.1323+0.3456i; ε_{zz}=9.045+0.0644i). The resonance is found for a value L~3.2 μm.

S12. Calculation of the limiting values for the formation of a focal spot.

In this section, we study the minimum and maximum achievable focal distances for in-plane high-$\vec{k}$ polaritons as a function of the incident wavelength λ_0 for most of the in-plane hyperbolic Reststrahlen band (from 10.5 μm to 11.6 μm). To do that, we perform numerical simulations employing a simple model based on two point dipoles separated by a distance d on a 165-nm-thick α-MoO_3 slab on a SiO_2 substrate. The dipoles act as launchers of in-plane polaritons with Poynting vector $\vec{S}$ yielding a focal spot upon their constructive interference (see inset to Fig. S16A). The wavelength-dependent focal distance (F) is eventually dictated by the wavelength-dependent angle of the propagating in-plane high-$\vec{k}$ polaritons with respect to the [100] direction in α-MoO_3 (θ), along which the density of propagating polaritonic modes is maximum (see section S1). On the other hand, the length from the dipoles to the focal spot can be easily calculated as $L = \frac{d}{2 \cdot sin\theta}$, and the total propagation length of the highly directional polaritons is defined as $L_T = L_P \cdot e$, being L_P the propagation length of the polaritons (see section S13). In order to obtain a focal spot the condition $L_T \geq L$ must be satisfied.

In Fig. S16A, we represent the values of L and L_T as a function of the illuminating wavelength λ_0 for different distances *d* between the point dipoles. Interestingly, whereas focusing can be obtained in the whole wavelengths range for a distance *d*=0.1 μm (black solid line in Fig. S16A), we find the respective minimum wavelengths threshold for the cases of *d*>0.1 μm (dashed black circles in Fig. S16A). As it meets the condition $L_T \geq L$, we can obtain a focal spot of polaritons in the wavelengths range marked with a shaded grey region in Fig. S16A. We note that the higher threshold for all *d* values is given by the TO phonon resonance delimiting the higher limit of the Reststrahlen band.

In Fig. S16B, we represent the minimum achievable focal distance F_{min} as a function of *d*, being the focal distances calculated as $F = \frac{d}{2 \cdot tan\theta}$. We highlight that a value as low as around 30 nm can be obtained for *d*=0.1 μm.

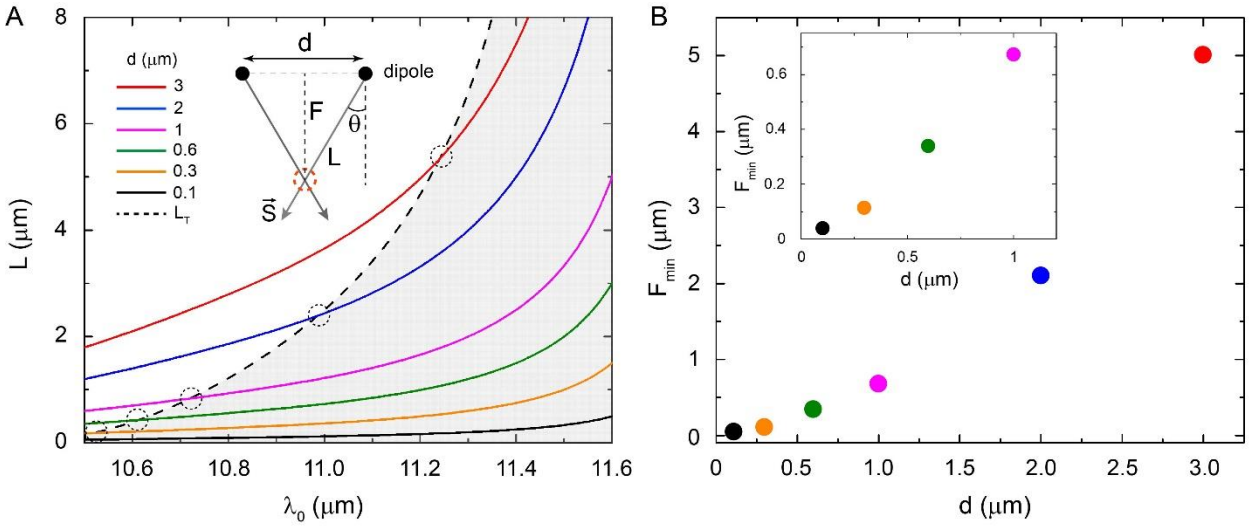

Fig. S16.- Achievable focal distances in α-MoO_3 employing two point dipoles as launchers of in-plane PhPs. (A) Length L as a function of the illuminating wavelength λ_0 (spanning the in-plane hyperbolic Reststrahlen band) for different separation distances d between two point dipoles launching in-plane high-$\vec{k}$ polaritons with Poynting vector ($\vec{S}$). The total propagation of the polaritons, L_T, is represented by the dashed black curve. The inset shows the geometrical relationship between the distance L from each of the dipoles to the focal spot (red dashed circle), the focal distance F and propagation direction of the polaritons forming an angle θ with respect to the [100] direction in α-MoO_3. The shadowed region marks the wavelengths range for which focusing of polaritons is obtained where $L_T \geq L$ (threshold wavelengths are marked with a dashed black circle). **(B)** Minimum achievable focal distance F_{min} as a function of the inter-distance d between the two point dipoles. The inset shows a zoom for d values up to 1 μm.

S13. Calculation of the propagation length of high-$\vec{k}$ polaritons in α-MoO_3.

The wavevector $\vec{k}$ and propagation length L_p of polaritons in α-MoO_3 are highly dependent on the direction of propagation. Here we calculate the propagation length L_p of high-$\vec{k}$ polaritons in α-MoO_3 along the in-plane direction which features the maximal density of optical states (see Fig. S1). To do so, we first assume that the imaginary part of the wavevector is parallel to the Poynting vector $\vec{S}$, i.e., is given by the vector (S_x, S_y) which in turn is perpendicular to the IFC, given by the real part of the wavevector $\mathrm{Re}(k)$. This assumption is reasonable, since the imaginary part of the wavevector is related to the decay of polaritons, which happens along its direction of propagation, given by the Poynting vector.
On the other hand, the polaritonic wavevector in a hyperbolic slab is given by Eq. 29:

$$k(\omega) = \frac{\rho}{k_0 d}\left[\arctan\left(\frac{\varepsilon_1 \rho}{\varepsilon_z}\right) + \arctan\left(\frac{\varepsilon_2 \rho}{\varepsilon_z}\right) + \pi l\right], \qquad l = 0, 1, 2 \ldots,$$

where k is the in-plane wavevector ($k^2 = k_x^2 + k_y^2$), l is the counting number of the mode, ε_1 and ε_2 are the permittivities of the superstrate (air) and substrate (SiO_2), respectively, d is the thickness of the slab and $\rho = i\sqrt{\varepsilon_z/(\varepsilon_x \cos^2\varphi + \varepsilon_y \sin^2\varphi)}$. In the latter, φ is the angle between the x-axis

([001] direction in $\alpha-MoO_3$) and the in-plane wavevector. By sweeping φ between 0 and 2π, we can calculate the polaritonic IFC, which has a hyperbola-like shape in the studied frequency range that can be approximated by the expression:

$$\frac{q_x^2}{\varepsilon_{y\,eff}} + \frac{q_y^2}{\varepsilon_{x\,eff}} = 1 \qquad (30)$$

Applying simple geometrical arguments, we can calculate the normal vectors to the hyperbola given by Eq. (30). Hence, we can easily find the angle θ between the propagation direction of the high-$\vec{k}$ polaritons (Poynting vector) with respect to the x-axis ([100] crystalline direction in α-MoO_3), which is given by:

$$\cot\theta = \frac{S_x}{S_y} = \frac{\varepsilon_x}{\varepsilon_y}\frac{k_x}{k_y} = \frac{\varepsilon_x}{\varepsilon_y}\cot\varphi \qquad (31)$$

The real and imaginary parts of the wavevector can be calculated from the dispersion relation, $\frac{q_x^2}{\varepsilon_{yeff}} + \frac{q_y^2}{\varepsilon_{x\,eff}} = 1$ (see definitions of ε_{xeff} and ε_{yeff} in page 6, section S1). In case of small losses ($\varepsilon_i'' \ll \varepsilon_i'$, being ε_i'' and $\varepsilon_i'$the imaginary and real parts, respectively), the real and imaginary parts of the wavevector could be found as:

$$\mathrm{Re}[q] = \frac{2\varepsilon}{k_0 d\varepsilon_x}\frac{1}{\sqrt{\cos^2\varphi - \frac{\varepsilon_y'}{\varepsilon_x'}\sin^2\varphi}}, \qquad (32)$$

$$\mathrm{Im}[q] = -\mathrm{Re}[q]\frac{\frac{\varepsilon_x''}{\varepsilon_x'}\cos^2\theta - \frac{\varepsilon_y'}{2\varepsilon_x'}\left(\frac{\varepsilon_x''}{\varepsilon_x'} + \frac{\varepsilon_y''}{\varepsilon_y'}\right)\sin^2\theta}{\cos\theta\cos\varphi + \frac{\varepsilon_y'}{\varepsilon_x'}\sin\theta\sin\varphi}, \qquad (33)$$

where q is the normalized wavevector $q = k/k_0$, with $k_0 = \omega/c$ the free-space light wavevector, and $\varepsilon = \frac{\varepsilon_1+\varepsilon_2}{2}$. Finally, the propagation length can be calculated as $L_p = 1/\mathrm{Im}[q]$.